Design and Mechanistic Study of Highly-durable Carbon Coated Cobalt Diphosphide Core-shell Nanostructure Electrocatalyst for the Efficient and Stable Oxygen Evolution Reaction

ACS APPLIED MATERIALS & INTERFACES

Energy, Environmental, and Catalysis Applications

Design and Mechanistic Study of Highly-durable Carbon Coated Cobalt Diphosphide Core-shell Nanostructure Electrocatalyst for the Efficient and Stable Oxygen Evolution Reaction

Merfat M. Alsabban, Xiulin Yang, Wandi Wahyudi, Jui-Han Fu, Mohamed Nejib Hedhili, Jun Ming, Chih-Wen Yang, M. Amtiaz Nadeem, Hicham Idriss, Zhiping Lai, Lain-Jong Li, Vincent C. Tung, and Kuo-Wei Huang

ACS Appl. Mater. Interfaces, **Just Accepted Manuscript** • DOI: 10.1021/acsami.9b01847 • Publication Date (Web): 16 May 2019

ACS Publications

is published by the American Chemical Society. 1155 Sixteenth Street N.W., Washington, DC 20036

Design and Mechanistic Study of Highly-durable Carbon Coated Cobalt Diphosphide Core-shell Nanostructure Electrocatalyst for the Efficient and Stable Oxygen Evolution Reaction

Merfat M. Alsabban,[a,b,c] Xiulin Yang,[a,b] Wandi Wahyudi,[a] Jui-Han Fu,[a] Mohamed. N. Hedhili,[d] Jun Ming,[a] Chih-Wen Yang,[a,b] Muhammad A. Nadeem,[e] Hicham Idriss,[e] Zhiping Lai,[a,f] Lain-Jong Li,[a,g,*] Vincent Tung,[a,b,*] and Kuo-Wei Huang,[a,b,*]

[a]Division of Physical Sciences and Engineering, King Abdullah University of Science and Technology, Thuwal, 23955-6900, Kingdom of Saudi Arabia

[b]KAUST Catalysis Center, King Abdullah University of Science and Technology, Thuwal, 23955-6900, Kingdom of Saudi Arabia

[c]Department of Chemistry, University of Jeddah, Jeddah, 21959, Kingdom of Saudi Arabia

[d]Core Labs, King Abdullah University of Science and Technology, Thuwal, 23955-6900, Kingdom of Saudi Arabia

[e]SABIC, Corporate Research and Innovation (KAUST), Kingdom of Saudi Arabia

[f]Advanced Membrane and Porous Materials Research Center, King Abdullah University of Science and Technology, Thuwal, 23955-6900, Kingdom of Saudi Arabia

[g]School of Materials Science and Engineering, University of New South Wales, Sydney 2052 Australia

*Email: L.Li@unsw.edu.au (L.-J. L.); vincent.tung@kaust.edu.sa (V.T.) and hkw@kaust.edu.sa (K.-W.H.)

Abstract

Facile synthesis of hierarchically functional, catalytically active, and electrochemically stable nanostructures holds tremendous promise for catalyzing efficient and durable oxygen evolution reaction (OER), yet remains a formidable challenge. Herein, we report the scalable production of core-shell nanostructures comprised of carbon-coated cobalt diphosphide nanosheets, C@CoP_2, via three simple steps: (i) electrochemical deposition of Co-species; (ii) gas phase phosphidation, and (iii) carbonization of CoP_2 for catalytic durability enhancement. Electrochemical characterizations showed that C@CoP_2 delivers an overpotential of 234 mV, retains its initial activity for over 80 hours of continuous operation, and exhibits a fast OER rate of 63.8 mV dec^{-1} in base.

Keywords

Carbon coating, Cobalt diphosphide, Electrochemical catalyst, Oxygen evolution reaction (OER), Phosphidation.

Introduction

Fossil fuels have underpinned the ever-increasing development of global economic infrastructure for centuries, but a new wave of renewable energy strategies is being strongly driven by mitigating climate change, growing environmental conscience, and advancing technological forefronts.[1, 2] A myriad of "lighthouse strategies", including photovoltaics, wind turbine, and hydrogen fuels, seem poised to potentially enable the transition to renewable and low carbon energy resources in a foreseeable future.[3, 4, 5] Specifically, hydrogen is considered a versatile and clean energy carrier,[6] and can be electrochemically produced with a low carbon footprint water splitting.[7] The need to ensure efficient and economic overall water splitting has motivated the immense research interests in synthesizing highly efficient, electrochemically robust, and earth abundant non-precious metal electrochemical catalysts for driving the cathodic hydrogen evolution reaction (HER) and oxygen evolution reaction (OER).[8] Relevant to HER, a classic two-electron reduction reaction,[9] OER is far more complex and challenging as the process involves four sequential proton-coupled electron transfer steps in conjunction with formation of oxygen-oxygen bonding.[10]

Transition metal oxides or hydroxides are the current benchmarks for OER in base, with overall performance on a par with or even surpassing the commercial standard, IrO_2.[11, 12, 13] Alternatively, cobalt phosphides (CoP_x) has emerged as a promising candidate and is found to be bifunctional for driving both HER and OER.[14, 15] Wang et al. demonstrated a nanostructuring strategy that capitalizes on the three-dimensional (3D) and high aspect ratio design of arrays of CoP nanoneedles supported on CC via a low temperature, hydrothermal phosphidation, [16] delivering an intriguing bifunctionality of driving both OER and HER at overpotentials of 281 mV and -95 mV, respectively. The advantageous design of nanostructuring was further extended by Yu and co-workers through synthesizing the hybrid electrochemical catalyst made of hollow CoP nanoparticles and N-doped graphene.[17] The synergy between N-doping graphene and hollow architecture of CoP results in substantially improved HER and OER metrics in alkaline solution with stability. An overpotential of 1.58 V was achieved and was found to remain stable beyond 65 hours of continuous operations. Recently, Saadi and co-workers prepared CoP films by cathodic deposition of Co^{2+} and $H_2PO_2^-$ on copper substrates.[18] The surface orthophosphate species were subsequently eliminated upon initial HER cycle in an acidic medium, thus yielding an optimized stoichiometric ratio of Co:P to 1:1. The as-prepared CoP catalyst showed an overpotential of only -85 mV for driving HER at a current density of 10 mA cm^{-2} but increased to -100 mV after 24

hours of continuous operations. Meanwhile, without altering the chemical makeups, nanostructured CoP via hydrothermal routes was found to deliver efficient OER characteristics.[19] Specifically, an overpotential of 320 mV was achieved in 1 M $KOH_{(aq)}$ for OER in conjunction with a steady electrochemical output stability up to 12 hours. These excellent OER metrics are comparable to the current commercial standard of IrO_2 and are attributed to the formation of an ultrafine and highly crystallized cobalt oxide (Co_2O_3) layer that acts as a protection layer for underlying CoP catalysts.

The bold conceptual design of implementing nanostructured CoP as the efficient bifunctional catalysts for driving both HER and OER, while promising, also raises considerable concerns from the mechanistic perspectives.[18, 20] First and foremost, such a bifunctional catalyst often requires a pre-activation process, i.e., a few cycles of electrochemical scans before arriving at steady and optimized OER metrics. Second, it is known that metal phosphides are susceptible to oxidation, especially under oxidizing potentials, leading to the formation of core-shell structures where spatially distributed and catalytically more active surface oxides overshadow the underlying phosphides. The undefined role of true catalytic species within these binary composites also makes future refinements in terms of OER metrics extremely difficult. Finally, to have widespread impact, the synthetic process should be high throughput and industrially scalable without the need for specialized processing equipment.[14] Herein, we address these limitations through the use of a potentially scalable CVD strategy to systematically control the sequential formation of ternary composites made of CoP_2 and a thin carbonaceous protection layer on highly conductive CC substrates, termed as C@CoP_2/CC. The premise for our design is to employ the CVD strategy to enable the stoichiometric tuning and phase engineering of CoP_2 OER catalyst in an epitaxial fashion, followed by subsequent deposition of carbonaceous protection layers to generate an unique core-shell architecture with well-defined interfaces to suppress the random surface oxidation of CoP_2 during OER in base while enhancing the electrochemical durability and operational stability.[21] This allows us to unambiguously determine the role of each component during OER through detailed morphological analyses in tandem with the surface-sensitive structural characterizations, including X-ray photoelectron spectroscopy (XPS) and Raman spectroscopy.[9] We demonstrate here that C@CoP_2/CC system exhibits an excellent activity and long-term durability, at which a catalytic current density of 10 mA cm^{-2} can be achieved at an overpotential of only 234 mV in 1M $KOH_{(aq)}$, and a minor degradation from its initial current

density over a prolonged period of continuous operation, tested for up an 80 hours. Furthermore, the unique core-shell architecture with well-defined interfaces between CoP_2 and C, in contrast to that previously reported where CoP_2 and C randomly tile or intersperse to form alloy-like interfaces, gave OER rate with a small Tafel slope of 63.8 mV dec^{-1}. These results clearly indicate that core-shell structured C@CoP_2/CC rivals or even surpasses most of the OER electrocatalyst, including CoP/C,[19] CoP/rGO-400,[22] and CoP_h/NG,[17] when measured in base. The morphologies and compositions of the catalysts vary with synthesis temperature and correlation between materials structures, electronic properties and electrocatalytic activities forms the basis accounted for the enhanced OER activity, durability, and stability.

Results and Discussion

Catalyst synthesis and characterizations

The nanostructured C@CoP_2/CC were synthesized through a three-step process. First, $Co(NO_3)_{2(aq)}$ solution precursor was used to electrochemically deposit Co-species on CC supporting substrate at -10 mA cm^{-2} for 20 min. Next, vapor phase phosphidation of $Co(OH)_2$/CC was carried out in vacuum within a modified CVD chamber using elemental red phosphorous as illustrated in Figure 1a. Prior to phosphidation process, furnace tube was purged with a mixture of $Ar_{(g)}$ (60 sccm) and $H_{2(g)}$ (20 sccm) for 30 min. Effect of phosphidation temperatures were examined in terms of various formed phases. It is found that phosphidation process starts at 450 °C with CoP phase formation. However, elevating the temperatures to 550 °C and 650 °C results in the formation of highly phosphorus cobalt phosphide phase, CoP_2. Annealing temperatures were progressively elevated beyond 550 °C to ensure the formation of CoP_2/CC. Importantly, the complete transformation of CoP_2 provides a chemically-defined and stoichiometrically controlled phase and thus enables the otherwise impossible mechanistic study of the roles of each component in driving OER. Lastly, the as-synthesized CoP_2/CC was conformally coated with an ultra-thin layer of carbonaceous shell (~2.2 nm) to afford a core (CoP_2/CC)-shell (C) architecture, thus further improving their stability against both harsh working environment and prolonged operation. X-ray diffraction (XRD) analysis was carried out to analyze phase composition, crystallinity, and particle size at various stages of annealing temperatures, as suggested in Figure 1b. A series of characteristic peaks from CC substrate, located at $2\theta = 25.8°$, 43.5° and 52.3°, can be assigned and are used as the reference for the following determination of each phase. On the basis of

characteristic XRD patterns (line in black), we identified and assigned electrochemically deposited Co on CC to $Co(OH)_2$/CC relative to the CoO/CC and CoP_x which are formed at higher annealing temperatures (see Table S1 for details). In general, increasing in phosphidation temperatures results in well-defined and sharp peaks, characteristics of increasing degree of crystallinity driven by interfacial surface energy minimization. Next, when annealed at 350 °C (line in red), $Co(OH)_2$ is further oxidized to form CoO whereas at 450 °C (line in blue), we began to observe the partial conversion of CoO into CoP. When the annealing temperature was further elevated to beyond 450 °C (line in pink for 550 °C and in green for 650 °C, respectively), pure phase and phosphorous-rich CoP_2 was formed and arranged in a monoclinic lattice arrangement as suggested in the computer-generated model (Figure 1c). Meanwhile, the average crystallite size as a function of the phosphidation temperatures was calculated using Scherrer equation (see Table S2 for details). Crystallite size evolution (τ) of as-prepared CoP_x formed at different temperatures is presented in Figure 1d. The empirical calculation meshes well with the experimental observation. As shown in the series of high-resolution transmission electron microscopy (HRTEM), the domain size of CoP_x crystallites formed at various stages of phosphidation temperatures was found to follow the similar trend, as higher phosphidation temperature leads to the growth of larger crystallites. (inset of Figure 1d). Initially, the domain size of CoP crystallite was found to be around 17 nm when reacted with phosphorus precursor at 450 °C and then continued to grow around 40 nm as the phosphidation temperature further increases to 650 °C. At 750 °C, saturated crystallite size is reached with no obvious changes are detected afterward.

In addition to the well-defined phase and crystallinity, morphological evolution, uniformity and coverage of the electrocatalysts was systematically explored through the use of scanning electron microscopy (SEM). Figure 2a first reveals the morphological evolution of pristine CC, electrodeposited $Co(OH)_2$/CC, and CoO/CC in tandem with CoP/CC and ultimately CoP_2/CC electrocatalyst prepared through phosphidation at different temperatures, ranging from 350 °C to 650 °C. After 20 minutes of electrochemical deposition in $Co(NO_3)_{2(aq)}$ solution, the initially smooth surface of pristine CC substrate is found to be fully covered with rugged-like structures of $Co(OH)_2$.[20] Next, dehydration of $Co(OH)_2$ after phosphidation at 350 °C results in the direct conversion to CoO while the rugged morphology remains intact. It is noted that $Co(OH)_2$ precursors seemed to strongly bind to the CC substrate fibers and no detachment was observed even after the phosphidation process which was held at 650 °C for hours. The inception of nano-

sized particles began to appear on the catalyst surface at 550 °C (highlighted in white dotted circles) and later merged into meandering ridges with neighboring rugs after phosphidation process was completed at 650 °C. In parallel, corresponding energy-dispersive X-ray (EDX) mapping of relevant elements, including Co in blue and P in green, closely resembling the spatially percolating ridges as demonstrated in Figure 2b. A closer look into the surface structure and morphology of CoP_2/CC (650 °C) is shown in Figure 2c which was carried by transmission electron microscopy (TEM). Additionally, the corresponding EDX elemental composition of the electrocatalyst was detected at different spots of a selected area and reveals the approximated chemical composition of Co/P ratio to be 1:2 (see Figure S1 for details).

XPS of the electrochemically deposited $Co(OH)_2$/CC and CoP_x/CC phases obtained at different phosphidation temperatures were collected and analyzed. For all samples, Co 2p, P 2p, O 1s, and C 1s were further analyzed with narrow scans after the survey mode (see Figure S2 for details). XPS of Co 2p is complex due to multiple chemical states, particle size effect, satellites, shell effects, energy loss, and overlap with its own Auger lines.[23, 24] In brief, the Co 2p of metallic Co is characterized by a doublet at 778 and 793 (with a split of 15 eV). That of Co^{2+} has binding energy positions at 780 and 795.5 eV and satellites at about 6 eV above each split and spin orbit splitting of 15.5 eV. The Co^{3+} binding energy position is at slightly lower binding energy position than that of Co^{2+} (by less than 1 eV) and has very weak satellites. XPS of Co cations in $Co(OH)_2$ are at a slightly higher binding energy position than that of CoO because of ligand effect. XPS of Co cations of Co_3O_4 is composed of signal for both Co^{2+} and Co^{3+} in a 1:2 ratio. With these in mind, the following data interpretation is given. In the case of $Co(OH)_2$/CC (see Figure S3a for details), the Co 2p core level spectrum displays two main peaks located at 781.4 eV and 797.3 eV corresponding to Co $2p_{3/2}$ and Co $2p_{1/2}$ doublet and their satellite peaks at 787.0 eV and 802.9 eV of Co^{2+} cations, respectively. At 450 °C (see Figure S3b for details), Co 2p spectrum shows four main peaks located at 778.8 eV, 781.8 eV, 793.8 eV and 798.2 eV along with broad satellite structures around ~ 786.6 eV and 803.2 eV. The sharp peaks at 778.8 eV and 793.8 eV correspond to Co $2p_{3/2}$ and Co $2p_{1/2}$ of metallic-like environment and is therefore attributed to Co atoms in CoP. The peaks at 781.8 eV, 798.2 eV, and their satellites around ~ 786.6 eV and 803.2 eV can be attributed to Co^{2+} cations of CoO and probably $Co(OH)_2$.[25]

Figures 2d and 2e present the XPS analysis of catalysts prepared at 550 ˚C and 650 ˚C phosphidation temperatures. The Co $2p_{3/2}$ peaks at 779.4 and P $2p_{3/2}$ at 129.2 eV become the dominant ones. There is no reference for XPS Co 2p of a well-defined CoP_2. Recent Bader charge analysis using DFT-GGA (as well as hybrid B3LYP method) indicated an almost pure covalent bond between Co and P with no local charge on each atom. Based on XRD and TEM analysis, where a pure CoP_2 phase is seen, it is highly likely that this splitting contains a contribution from Co cations of CoP_2. The P 2p core level is fitted using one doublet positioned at 129.2 eV and 130.0 eV attributed to P ions in CoP_2, along with one broad peak centered at 134.8 eV corresponding to a more oxidized form of phosphorus (most likely PO_4^{3-}).[26]

Next, to make the core-shell nanostructure, CoP_2/CC was directly reacted with glucose and then annealed at 350 °C within a modified CVD furnace with control over vacuum (<10 mTorr) at incremental heating steps (2.75 °C min^{-1}). A cross-sectional SEM image featuring a freestanding piece of C@CoP_2/CC (650 °C) mechanically exfoliated from the supporting CC substrates with an overall thickness around 341 nm (Figure S4a). Because of the well-defined interface between C@CoP_2 layers as suggested by a combination of high-resolution cross-sectional SEM and the corresponding line-scan EDX profile, spatial distribution of each element along the exfoliated C@CoP_2/CC (650 °C) can be evidentially identified (Figure S4b). It is noted that the spatial distribution of C is largely confined in the top layer of the composite electrodes. Since the CC supporting substrate was previously removed, the formation of conformal carbon coating on the surface of CoP_2 must stem from the reaction and subsequent transformation from glucose, thus validating our proposed design of core-shell architecture.

As suggested in Figure 3a and b, HRTEM analysis in tandem with electron energy loss spectroscopy (EELS) is conducted to confirm the thickness and to reveal the spatial distribution of carbon coating. Admittedly, it becomes apparent that the coating of carbon layer is determined to be ~2.2 nm and is uniformly deposited on CoP_2 nanoparticles. To infer the transport across the core/shell nanoarchitecture, Figure 3c shows the electrochemical impedance spectroscopy (EIS) of the electrolysis cells for both pristine CoP_2/CC and C@CoP_2/CC. The intercept on the real axis in the high frequency range is associated with series resistance (R_s) of the electrolyte and electrical contacts in electrochemical system. The first semi-circle corresponds to the charge-transfer resistance (R_{CE}) at the electrode/electrolyte interface, where the second semi-circle is attributed to the charge-transfer resistance (R_{CT}) at the electrodes. It is clearly shown that the carbon layer on

the CoP_2 significantly lower both ohmic resistance (1.5 Ω, R_s) and charge transfer resistance (4.7 Ω, R_{CE}+R_{CT}), whereas pristine CoP_2 shows higher resistance of 2.9 Ω and 5.4 Ω, respectively. To put our design of core-shell architecture into a further test, we conducted an XPS study to systematically monitor the temporal evolution of surface oxidation on both pristine CoP_2/CC and C@CoP_2/CC. For a fair comparison, both specimens were placed at ambient conditions without further protection. Figure 3d presents a series of unprotected sample in which the binding energy position of Co $2p_{3/2}$ of Co^0 is given (778.0 eV) as a reference. The experimentally observed Co $2p_{3/2}$ is about 1 eV above. The spin orbit splitting of the sharp signals of P $2p_{3/2,\ 1/2}$ is found to be of ca. 14.6 eV. Weak structures (arrows indicated on the 0 days spectrum) indicate the presence of some satellites contribution. Upon leaving the sample in ambient air, some oxidation occurs. This can be seen by the development of a signal at about 781.5 eV (2 days) that further broadened with time (8 days and above) in addition to the development of another signal about 5 eV above. The position of this peak (and that at ca. 798 eV) is similar to that of Co hydroxide (spin orbit split of ca. 15.7 eV). The increasing signal of these states, with time, is thus due to surface oxidation of the last few layers (the escape depth, λ, of a photoelectron with a kinetic energy of ca. 800 eV is about 2 nm). The fact that the signal does not saturate even after 24 days is an indication of a slow oxidation process. Figure 3e presents the same data analysis for the carbon-protected sample. It is obvious that the extent of oxidation is attenuated due to the protection of a large fraction of the CoP_2 surface, probably because of surface hydroxyls diffusion is slowed down. Similar results have been obtained for the P 2p signal where in this case the signal due to highly oxidized P ions at 134 – 135 eV is attenuated (see Figures S5a and b for details). To further quantify the degree of oxidation in each sample, the relative ratio of oxidation relative to the freshly prepared CoP_2/CC as a function of duration of exposing to ambient conditions is plotted. Whereas the oxidation of CoP_2/CC peaks at 80% after 25 days, the thin carbonaceous coating effectively constitutes a shielding layer to suppress the further oxidation after its inception (Figure 3f).

Similar trends are also found in Raman spectroscopy (Figure 3g) in which two sharp and dominant peaks located at 1350 cm^{-1} and 1578 cm^{-1} are attributed to the characteristic D and G bands, respectively, and correlated to the carbonaceous species which can be clearly seen with peak position unchanged after 25 days, an indication of its chemical resilience. However, Raman spectrum of unprotected electrocatalyst clearly shows CoP_2 vibration modes in addition to two weak and broad peaks indexed to D and G bands from the carbon substrate. These results present

the utility of the protective nature which is provided by carbon shield layer into C@CoP_2 composite electrocatalyst which reflects minor air oxidation. Meanwhile, a series new peaks emerged in pristine CoP_2 after exposing to air for a long period of time, likely due to the formation of oxidation species and possible side reactions. Together, the data in Figure 3 confirm that formation of chemically resilient carbonaceous layer on top of the catalytically active but oxidatively vulnerable CoP_2. Below, using C@CoP_2 as the OER electrodes, we discuss the OER metrics and mechanistic study of the core-shell architectured C@CoP_2 catalyst.

Electrocatalytic activity in OER

Electrocatalytic OER activities of CoP_x electrocatalyst were examined in base (1M $KOH_{(aq)}$). Figure 4a displays linear sweep voltammetry (LSV) curves (the current density was normalized to the geometrical area of the CC substrate) of various CoP_x/CC OER electrodes phosphatized at various temperatures. In order to account for the solution resistance, the potential was measured after internal resistance (iR) correction. Among all CoP_x species formed, CoP_2/CC synthesized at 650 °C is found to be the most active phase toward OER, delivering overpotentials of 234 mV and 256 mV at 10 mA cm^{-2} and 20 mA cm^{-2}, respectively. The observed changes in the electrochemical catalytic performance is found to be dependent on the phosphidation temperature which is accordingly associated to the crystallinity and size of the particles. Based on the spectroscopic characterizations and TEM observations, the inception of the formation of crystallized CoP_2/CC only occurs when phosphatized temperature elevates above 450 °C and the growth in crystallite dimensions continues until 750 °C. Another important factor arises accompanied with the crystal growth is the formation of dense packing of individual crystallites, thus limiting the undesired gaps that are known to adversely affect the electrochemical catalyst due to the electrical constriction points and inferior crystallinity. Importantly, the substantially improved overpotentials measured from CoP_2/CC readily surpass the previously reported nanostructuring cobalt phosphide as well as those supported on conductive graphitic templates (see Table 1 for details). Further detailed insights into the OER kinetics in base were obtained through the extrapolation of slopes from Tafel plots shown Figure 4b. It can be seen that the Tafel slopes of CoP_2/CC attained in a high pH condition remain reasonably low (63.8 mV dec^{-1}), suggesting a fast OER kinetics stemmed from the structurally porous morphology of CoP_2. Indeed, electric double-layer capacitance (EDLC) of CoP_x phosphatized at various temperatures deduced from the dependence of capacitive currents at different scan rates (see Figure S6 for details) exhibited the enhanced unit electrode capacitance

with the increased phosphatized temperatures [27] as shown in Figure 4c. Comparing all CoP_x/CC electrocatalysts prepared at different temperatures, CV curves show that CoP_2/CC prepared at 650 °C gave the highest anodic and cathodic current densities. To further verify the catalytic species, a series of Co-based electrocatalysts were prepared and systematically examined in base for OER. These electrodes include $Co(OH)_2$/CC, Co_3O_4/CC, along with pristine and calcined CC (Figure 4d). Through comparing the LSV, it becomes apparent that Co_3O_4/CC and $Co(OH)_2$/CC, the oxidized products of CoP_2, are "OER active" and exhibit overpotentials of 322 mV and 293 mV at current densities of 10 mA cm^{-2}, respectively, while calcined and bare CC had insignificant activity toward OER. Whereas the exceedingly low overpotentials CoP_2/CC in base outweigh its oxidized counterparts and lead us to conclude that the formation of surface oxide layers, while OER active, will only degrade the overall OER performance, ruling out the synergy between CoP_2/CC, $Co(PO_3)_2$/CC, and Co_3O_4/CC during the OER reaction will require more systematic and comprehensive characterizations and is currently underway.

Comparable OER metrics were attained for C@CoP_2/CC relative to CoP_2/CC as shown in Figure 4e while C@CoP_2/CC only exhibited a mild decrease of output current density after 80 hours of continuous operation in base, an indication of the chemically resilient but electrically addressable nature of carbonaceous protection layer. Specifically, after incurring an initial decay of 20% of output current densities from the beginning of stability test (the first 20 hours of measurement), we only observed a very mild decrease in C@CoP_2/CC for the next 60 hours of continuous operation (Figure 4f).

Post-catalysis characterization

Figure 5a shows the post-catalytic XRD pattern of as-prepared catalyst at 650 °C in which cobalt phosphate $Co(PO_3)_2$ (JCPDS card no. 01-086-2161) along with the cobalt oxide Co_3O_4 (JCPDS card no. 00-043-1003) were observed. Moreover, weak and broad peaks indexed to monoclinic CoP_2 (JCPDS card no. 01-077-0263) were detected. These results suggest that a very limited amount of CoP_2 is oxidized and converted to both $Co(PO_3)_2$ and Co_3O_4 during electrolysis while the majority of CoP_2 remains intact under the protection of chemically resilient and electrically addressable carbonaceous coating layers. Further, XPS was used to elucidate the post-catalytic surface and near surface changes. Co 2p core level spectrum in Figure 5b shows two main peaks at 780 eV and 795.2 eV along with broad satellites around ~ 789.6 eV and 804.2 eV corresponding

to Co $2p_{3/2}$ and Co $2p_{1/2}$ of Co^{2+} and/or Co^{3+}, respectively.[5] Although, the weak satellite contribution may indicate that Co^{2+} contribution is minor. Consistently, P 2p peak at 133.1 eV of phosphate was observed indicating the surface oxidation of CoP_2 to $Co(PO_3)_2$.[28] Survey spectrum of post-catalytic sample shows the existence of Co, O, P, C, and K from $KOH_{(aq)}$ electrolyte solution (see Figure S7 for details). XRD, and XPS results are found to correlate with each other and confirm changes of catalyst surface to form amorphous cobalt oxy-species during water oxidation. Because of this transformation, we have tested the performance of $Co(PO_3)_2$. Figure 5c demonstrates a poor performance for $Co(PO_3)_2$ that was synthesized *in-situ* by oxidation of CoP_2/CC (650 °C). On the other hand, catalytic activity of Co_3O_4/CC synthesized by thermal oxidation process of electrodeposited $Co(OH)_2$/CC was comparable with CoP_2/CC (650 °C) (Figure 5d). Again, the catalytic activity of CoP_2/CC (650 °C) is higher than that of Co_3O_4/CC (350 °C). For better understanding of material preservation during water oxidation process, microstructures of pristine and shielded catalyst was investigated after prolonged operation in base (Figure 5e). As expected, un-protected catalyst suffers material dissolution, while carbon coated specimen shows compacted catalyst to carbon fibers even after long continuous operation.

Conclusions

In summary, we report a facile synthesis of C@CoP_2/CC core-shell nanostructures with electrochemically efficient and operationally durable OER characteristic in base. The formation of such core-shell nanostructures offers several important advantages. First, the facile synthesis through the use of a modified CVD enables the formation of catalytically active CoP_2/CC core and chemically inert and electrically addressable C shell to simultaneously circumvent the catalytic, kinetic, and dynamic hurdles for driving efficient and stable OER in base. Second, the core-shell nanostructures provide a well-defined model system to independently and conclusively infer the role of each component during OER through implementing a combination of structural, spectroscopic, and electrochemical characterizations. Third, the ease of modulating the stoichiometric ratios between Co and P through controlled reaction with red P allows us to unambiguously arrive at the conclusion: C@CoP_2 is the active species for OER. Electrochemical characterizations collectively indicate that C@CoP_2/CC outperforms any other non-precious metal based OER catalyst in its capability in delivering an overpotential of only 234 mV along with an improved Tafel slope of 63.8 mV dec^{-1} when measured in base. In parallel, C@CoP_2/CC can drive

OER in an electrochemical stable and consistent fashion over a long and continuous operation with a minor decay due to the formation of $Co(PO_3)_2$ and Co_3O_4 during water electrolysis process. Given the synthetic scalability, generality, and versatility of our modified CVD approach, we envision that a wide array of new OER catalysts with enhanced catalytic activity, operational stability and structural functionality can be rationally, rapidly, and readily designed. This shall in turn provide exciting opportunities for emerging applications beyond OER.

Acknowledgments

We thank King Abdullah University of Science and Technology (KAUST) for generous financial support. The work was in part funded by SABIC-CRD at KAUST, grant number OSR #3041. V. T. acknowledges the support from User Proposals (#4420 and #5067) at the Molecular Foundry, Lawrence Berkeley National Lab, supported by the Office of Basic Energy Sciences, of the U.S. Department of Energy under Contract No. DE-AC02-05CH11231.

Experimental

Materials

All chemicals including cobalt (II) nitrate hexahydrate ($Co(NO_3)_2.6H_2O$, ≥ 96 %), potassium hydroxide ($KOH_{(aq)}$, ≥ 85 %), red phosphorus (≥ 99.99 %) and ethanol (≥ 85 %) were purchased from Sigma-Aldrich and used without further purification. Water used was purified through a Millipore ultrapure water system (18.2 MΩ.cm at 25 °C).

Characterizations

The morphology of the catalysts and electron energy loss spectroscopy (EELS) was studied by field-emission scanning electron microscopy (FESEM, FEI Quanta 600). X-ray diffraction (XRD, Bruker D8 Discover diffractometer, using Cu Kα radiation, λ = 1.54 Å) was used to investigate the phase composition. Lattice structure was studied by transmission electron microscopy (FEI Titan ST, operated at 300 KV) while electronic structure and surface/near surface composition is studied by XPS using a Kratos Axis Ultra DLD spectrometer equipped with a monochromatic Al Kα X-ray source ($h\nu$ = 1486.6 eV) operating at 150 W, a multi-channel plate and delay line detector at about 1.0 $x10^{-9}$ torr background pressure. All data were collected at 0° take-off angle in hybrid mode of electrostatic and magnetic lenses with aperture slot of 300 μm x 700 μm for spectra recording. Survey spectra was taken at fixed analyzer path energy of 160 eV, and 20 eV for high resolution spectra. C 1s peak sourced by the substrate (at 284.4 eV) of the sp^2 hybridized (C=C) was used as a binding energy reference. In order to avoid differential charging, all the samples were mounted in floating mode. All data was further analyzed by CasaXPS software. After excluding linear or Shirley type background, peaks were fitted using Gaussian (70%)–Lorentzian (30%) (GL30) function. Employment of Raman spectrometer LabRAMAramis (HoribaJobinYvon) was accomplished in the range of 100 – 2500 cm^{-1} in which an excitation source of a diode-pumped solid state (DPSS) laser is used with 473 nm wavelength at room temperature. In order to focus incident laser beam to a 1 μm spot diameter, a microscope with total of 1006 objective lens was used (Olympus BX 41). Si peak at 521 cm^{-1} was used for calibration.

Electrochemical Measurements

Eelectrochemical measurements were accomplished at room temperature on an electrochemical work station Biologic VMP3. OER performance was obtained by means of linear sweep voltammetry (LSV) at a scan rate of 0.05 mV s^{-1} in 1 M $KOH_{(aq)}$ (pH = 13.45) solution. RHE calibration in a hydrogen saturated electrolyte was accomplished with 1.00533 V offset, which

perfectly coincides with 0.99324 in Nernst equation (E(RHE) = E(Ag/AgCl) + 0.99324). Graphite rod and Ag/AgCl (in 3 M KCl solution) were used as a counter and reference electrodes, respectively.

Electrochemical deposition of Co-species on carbon cloth

CC with a size of 3 cm × 1.0 cm was used as a conductive substrate. It was washed with ethanol and deionized water continually to remove impurities. CC of 2.0 cm^2 geometric area was then immersed into 0.1 M $Co(NO_3)_{2(aq)}$ solution for electrodeposition process of Co. The Pt foil and Ag/AgCl (in 3 M $KCl_{(aq)}$ solution) electrodes were used as counter and reference electrodes, respectively. Electrodeposition of Co was performed at constant current of -10 mA cm^{-2} for 20 min. In order to promote the vapor phase phosphidation process, as-prepared samples were exposed to air to form oxide and hydroxide surface layer with Co loading amount of ~ 2.22 mg cm^{-2} (Figure S8).

Synthesis of CoP_x by vapor phase phosphidation

The phosphidation process was performed in a close-ended tube fixed inside the tube furnace containing red phosphorus and electrodeposited cobalt on a CC substrate. Prior to the phosphidation, tube furnace was pumped and purged with $Ar_{(g)}$ (60 sccm) and $H_{2(g)}$ (20 sccm) for 30 min (~ 12 torr) to completely remove oxygen from the system. Lastly, phosphidation process was carried out under vacuum. It is found that cobalt phosphide and cobalt diphosphide form on CC at different temperatures ranging between 450 °C to 650 °C for 30 min duration and heating rate of 15 °C min^{-1}. The loading amount of as-prepared electrocatalyst on CC was determined, after drying in a vacuum oven, to be 5.59 ± 0.9 mg cm^{-2} by using of a high accuracy weighing balance as suggested in Table S3).

Preparation of carbon coated cobalt phosphide on CC

The pristine CoP_2/CC was immersed in 5 mg mL^{-1} glucose solution for 8 h, then dried at room temperature. The glucose coated cobalt diphosphide was then loaded into a tube furnace and pumped under vacuum (<10 mTorr), followed by calcination at 350 °C for 1 h with heating rate of 2.75 °C min^{-1}.

Preparation of Co_3O_4 on CC

Co_3O_4 nanosheets were synthesized through thermal oxidation process, in which $Co(OH)_2$/CC was placed into a tube furnace and calcined at 350 °C for 2 h in air at heating rate of 2.75 °C min^{-1}.

Reference electrode calibration

1M $KOH_{(aq)}$ electrolyte solution was purged with hydrogen gas for 30 min prior the measurements. Pt wires, and Ag/AgCl (in 3 M $KCl_{(aq)}$ solution) were used as counter, working, and reference electrodes, respectively. Current-voltage (CV) curves were obtained at a scan rate of 5 mV s^{-1}. Thermodynamic potential of the hydrogen electrode reactions was then taken at the zero current crossing the average of the two potentials (Figure S9). The result shows that E(Ag/AgCl) is lower than E(RHE) by 1.00533 V.

Supporting information

STEM-EDX pattern, XPS survey spectrum, narrow scan XPS spectrum, cross-sectional SEM and EDX line scans, EDLC measurements, electrochemical deposition digital display, RHE voltage calibration (Figures S1-S9) and XRD data, particles size, and catalyst loading amount on CC (Table S1-S3).

References

(1) Sun, Y. J.; Bigi, J. P.; Piro, N. A.; Tang, M. L.; Long, J. R.; Chang, C. J. Molecular Cobalt Pentapyridine Catalysts for Generating Hydrogen from Water. J. Am. Chem. Soc. 2011, 133, 9212-9215.

(2) Fang, Z. W.; Peng, L. L.; Qian, Y. M.; Zhang, X.; Xie, Y. J.; Cha, J. J.; Yu, G. H. Dual Tuning of Ni-Co-A (A = P, Se, O) Nanosheets by Anion Substitution and Holey Engineering for Efficient Hydrogen Evolution. J. Am. Chem. Soc. 2018, 140, 5241-5247.

(3) Cobo, S.; Heidkamp, J.; Jacques, P. A.; Fize, J.; Fourmond, V.; Guetaz, L.; Jousselme, B.; Ivanova, V.; Dau, H.; Palacin, S.; Fontecave, M.; Artero, V. A Janus Cobalt-Based Catalytic Material for Electro-splitting of Water. Nat. Mater. 2012, 11, 802-807.

(4) Lewis, N. S.; Nocera, D. G. Powering the Planet: Chemical Challenges in Solar Energy Utilization. Proc. Natl. Acad. Sci. U.S.A. 2006, 103, 15729-15735.

(5) Ahn, H. S.; Tilley, T. D. Electrocatalytic Water Oxidation at Neutral pH by a Nanostructured $Co(PO_3)_2$ Anode. Adv. Funct. Mater. 2013, 23, 227-233.

(6) Eppinger, J.; Huang, K. W. Formic Acid as a Hydrogen Energy Carrier. Acs Energy Lett. 2017, 188-195.

(7) Jiang, P.; Liu, Q.; Liang, Y. H.; Tian, J. Q.; Asiri, A. M.; Sun, X. P. A Cost-Effective 3D Hydrogen Evolution Cathode with High Catalytic Activity: FeP Nanowire Array as the Active Phase. Angew. Chem. Int. Ed. 2014, 53, 12855-12859.

(8) Yang, X. L.; Lu, A. Y.; Zhu, Y.; Min, S. X.; Hedhili, M. N.; Han, Y.; Huang, K. W.; Li, L. J. Rugae-like FeP Nanocrystal Assembly on a Carbon Cloth: an Exceptionally Efficient and Stable Cathode for Hydrogen Evolution. Nanoscale 2015, 7, 10974-10981.

(9) Chen, Y. C.; Lu, A. Y.; Lu, P.; Yang, X. L.; Jiang, C. M.; Mariano, M.; Kaehr, B.; Lin, O.; Taylor, A.; Sharp, I. D.; Li, L. J.; Chou, S. S.; Tung, V. Structurally Deformed MoS_2 for Electrochemically Stable, Thermally Resistant, and Highly Efficient Hydrogen Evolution Reaction. *Adv. Mater*. 2017, 29, 1703863- 1703873.

(10) Zhou, S.; Liu, N. S.; Wang, Z. Y.; Zhao, J. J. Nitrogen-Doped Graphene on Transition Metal Substrates as Efficient Bifunctional Catalysts for Oxygen Reduction and Oxygen Evolution Reactions. ACS Appl. Mater. Interfaces 2017, 9, 22578-22587.

(11) Yang, X. L.; Li, H. N.; Lu, A. Y.; Min, S. X.; Idriss, Z.; Hedhili, M. N.; Huang, K. W.; Idriss, H.; Li, L. J. Highly Acid-Durable Carbon Coated Co_3O_4 Nanoarrays as Efficient Oxygen Evolution Electrocatalysts. Nano Energy 2016, 25, 42-50.

(12) Liu, W.; Liu, H.; Dang, L. N.; Zhang, H. X.; Wu, X. L.; Yang, B.; Li, Z. J.; Zhang, X. W.; Lei, L. C.; Jin, S. Amorphous Cobalt-Iron Hydroxide Nanosheet Electrocatalyst for Efficient Electrochemical and Photo-Electrochemical Oxygen Evolution. Adv. Funct. Mater. 2017, 27, 1603904-1603913.

(13) Gao, X. H.; Zhang, H. X.; Li, Q. G.; Yu, X. G.; Hong, Z. L.; Zhang, X. W.; Liang, C. D.; Lin, Z. Hierarchical $NiCo_2O_4$ Hollow Microcuboids as Bifunctional Electrocatalysts for Overall Water-Splitting. Angew. Chem. Int. Ed. 2016, 55, 6290-6294.

(14) Shi, Y. M.; Zhang, B. Recent Advances in Transition Metal Phosphide Nanomaterials: Synthesis and Applications in Hydrogen Evolution Reaction. Chem. Soc. Rev. 2016, 45, 1529-1541.

(15) Mahmood, N.; Yao, Y. D.; Zhang, J. W.; Pan, L.; Zhang, X. W.; Zou, J. J. Electrocatalysts for Hydrogen Evolution in Alkaline Electrolytes: Mechanisms, Challenges, and Prospective Solutions. Adv. Sci. 2018, 5, 1700464-1700486.

(16) Wang, P.; Song, F.; Amal, R.; Ng, Y. H.; Hu, X. L. Efficient Water Splitting Catalyzed by Cobalt Phosphide-Based Nanoneedle Arrays Supported on Carbon Cloth. ChemSusChem 2016, 9, 472-477.

(17) Yu, X. B.; Zhang, S.; Li, C. Y.; Zhu, C. L.; Chen, Y. J.; Gao, P.; Qi, L. H.; Zhang, X. T. Hollow CoP Nanopaticle/n-doped Graphene Hybrids as Highly Active and Stable Bifunctional Catalysts for Full Water Splitting. Nanoscale 2016, 8, 10902-10907.

(18) Saadi, F. H.; Carim, A. I.; Verlage, E.; Hemminger, J. C.; Lewis, N. S.; Soriaga, M. P. CoP as an Acid-Stable Active Electrocatalyst for the Hydrogen-Evolution Reaction: Electrochemical Synthesis, Interfacial Characterization and Performance Evaluation. J. Phy. Chem. C 2014, 118, 29294-29300.

(19) Chang, J. F.; Xiao, Y.; Xiao, M. L.; Ge, J. J.; Liu, C. P.; Xing, W. Surface Oxidized Cobalt-Phosphide Nanorods As an Advanced Oxygen Evolution Catalyst in Alkaline Solution. ACS Catal. 2015, 5, 6874-6878.

(20) Yang, X. L.; Lu, A. Y.; Zhu, Y. H.; Hedhili, M. N.; Min, S. X.; Huang, K. W.; Han, Y.; Lin, L. J. CoP Nanosheet Assembly Grown on Carbon Cloth: A Highly Efficient Electrocatalyst for Hydrogen Generation. Nano Energy 2015, 15, 634-641.

(21) Zhou, S.; Yang, X. W.; Pei, W.; Liu, N. S.; Zhao, J. J. Heterostructures of MXenes and N-doped Graphene as Highly Active Bifunctional Electrocatalysts. Nanoscale 2018, 10, 10876-10883.

(22) Jiao, L.; Zhou, Y. X.; Jiang, H. L. Metal–Organic Framework-based CoP/reduced Graphene Oxide: High-Performance Bifunctional Electrocatalyst for Overall Water Splitting. Chem. Sci. 2016, 7, 1690-1695.

(23) Lukashuk, L.; Yigit, N.; Rameshan, R.; Kolar, E.; Teschner, D.; Havecker, M.; Knop-Gericke, A.; Schlogl, R.; Fottinger, K.; Rupprechter, G. Operando Insights into CO Oxidation on Cobalt Oxide Catalysts by NAP-XPS, FTIR, and XRD. ACS Catal. 2018, 8, 8630-8641.

(24) Bazylewski, P.; Boukhvalov, D. W.; Kukharenko, A. I.; Kurmaev, E. Z.; Hunt, A.; Moewes, A.; Lee, Y. H.; Cholakh, S. O.; Chang, G. S. The Characterization of Co-Nanoparticles Supported on Graphene. RSC Adv. 2015, 5, 75600-75606.

(25) Liu, Q.; Tian, J. Q.; Cui, W.; Jiang, P.; Cheng, N. Y.; Asiri, A. M.; and Sun, X. P. Carbon Nanotubes Decorated with CoP Nanocrystals: A Highly Active Non-noble-metal Nanohybrid Electrocatalyst for Hydrogen Evolution. Angew. Chem. Int. Ed. 2014, 53, 6710-6714.

(26) Rodriguez-Aguado, E.; Infantes-Molina, A.; Cecilia, J. A.; Ballesteros-Plata, D.; Lopez-Olmo, R.; Rodriguez-Castellon, E. Co_xP_y Catalysts in HDO of Phenol and Dibenzofuran: Effect of P content. Top. Catal. 2017, 60, 1094-1107.

(27) Trasatti, S.; Petrii, O. A. Real Surface Area Measurments in Electrochemistry. J. Electroanalytical Chem. 1992, 327, 353-376.

(28) Kanan, M. W.; Nocera, D. G. In Situ Formation of an Oxygen-Evolving Catalyst in Neutral Water Containing Phosphate and Co^{2+}. Science 2008, 321, 1072-1075.

(29) Wang, J. M.; Yang, W. R.; Liu, J. Q. CoP_2 Nanoparticles on Reduced Graphene Oxide Sheets as a Super-Efficient Bifunctional Electrocatalyst for Full Water Splitting. J. Mater. Chem. A 2016, 4, 4686-4690.

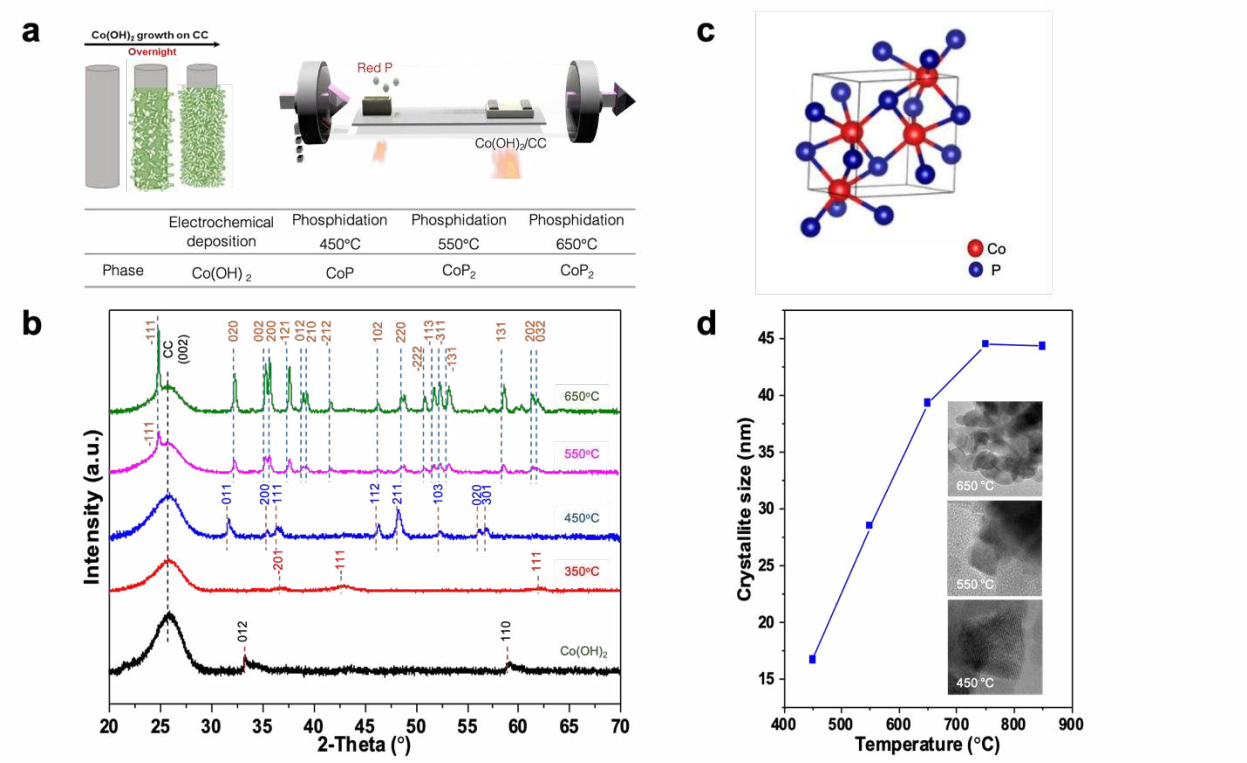

Figure 1. (a) Schematic illustration depicts the synthesis of CoP_2 through: (i) electrochemical deposition of Co-species on CC, (ii) followed by reacting of $Co(OH)_2$ with elemental red P powders along with a summary of different phases formed as a function of phosphidation temperature. (b) Temperature-dependent XRD characterizations suggest the incremental conversion of $Co(OH)_2$/CC to CoO/CC at 350 °C, followed by gradual transformation to CoP/CC at 450 °C, and final formation of CoP_2/CC beyond 550 °C. (c) A computer generated model shows the monoclinic CoP_2 crystal structure. (d) Dimensions of CoP_2 crystallite size increase monotonically after transformation reaction initiates at 450˚C. Inset shows a series of TEM images of CoP_x crystallites formed at different phosphidation temperatures.

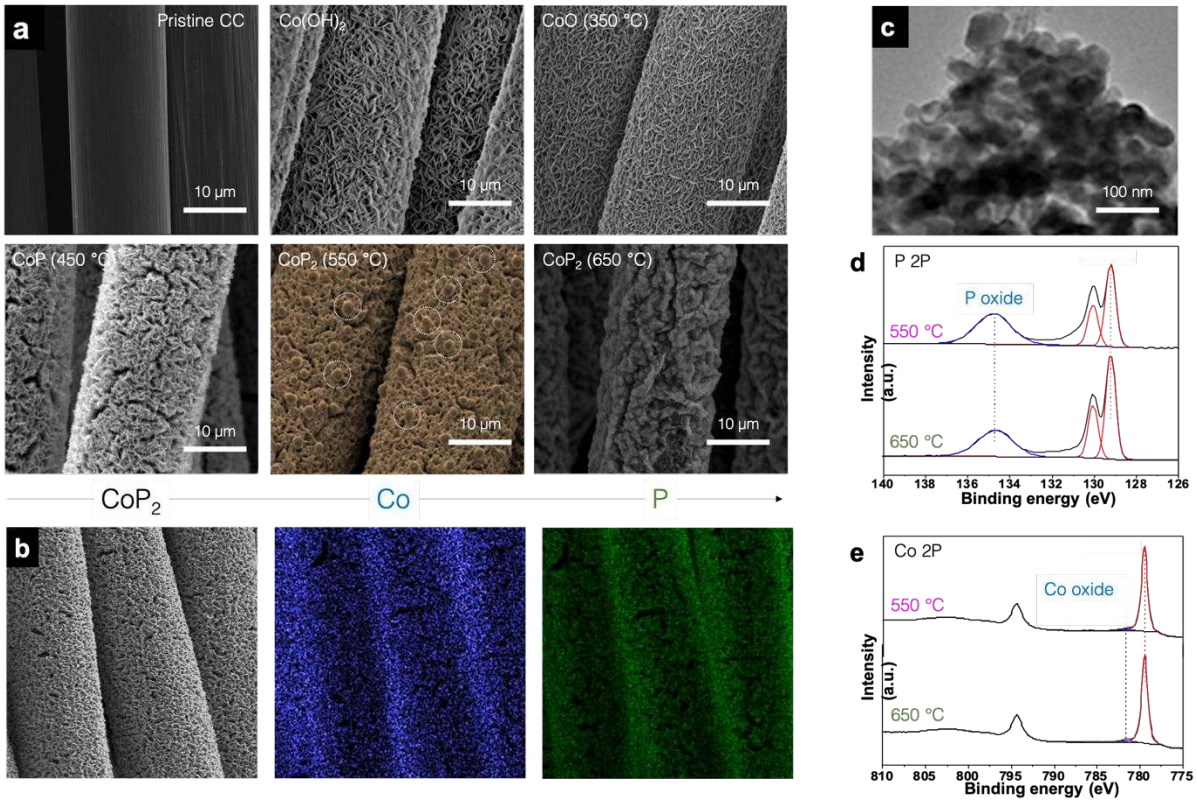

Figure 2. (a) Representative SEM images show different stages of temperature-dependent phase evolution, ranging from pristine CC, $Co(OH)_2$/CC, CoO/CC, CoP/CC and finally CoP_2/CC during phosphidation process. (b) SEM image and the corresponding EDX elemental mapping of CoP_2/CC after phosphidation at 650 °C, including Co (color in blue), and P (color in green), reveal the complete coverage and uniformity in conjunction with spatial homogeneity of each element. (c) STEM image of CoP_2/CC after phosphidation at 650 °C. Narrow scan XPS spectra for: (d) Co 2p and (e) P 2p of CoP_2/CC formed at 550 °C and 650 °C.

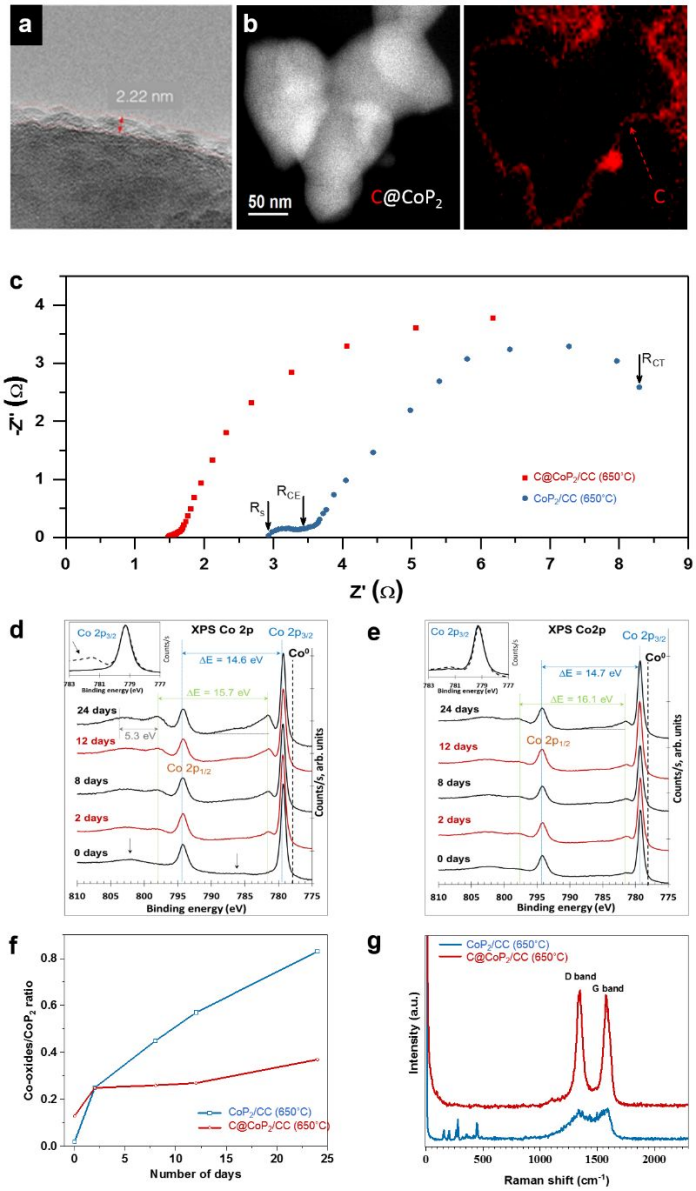

Figure 3. (a) HRTEM image of C@CoP_2/CC (phosphatized at 650 °C) reveals the conformal and uniform coating of carbon layers with thickness of ~2.2 nm. (b) EELS mapping of C shell of C@CoP_2/CC (phosphatized at 650 °C) clearly shows the well-defined interface. (c) EIS of electrocatalysis cell of pristine CoP_2/CC and C@CoP_2/CC (650 °C) further demonstrates the improved transport characteristics across the core/shell nanoarchitecture. Narrow scan XPS spectra for Co $2p_{3/2}$ of (d) pristine CoP_2/CC (650 °C), (e) C@CoP_2/CC (650 °C) for freshly-prepared samples and after being exposed to air. (f) Relative degree of oxidation as function of air exposure time of pristine CoP_2/CC (650 °C) and C@CoP_2/CC (650 °C). (g) Raman spectra of pristine CoP_2/CC (650 °C) and C@CoP_2/CC (650 °C).

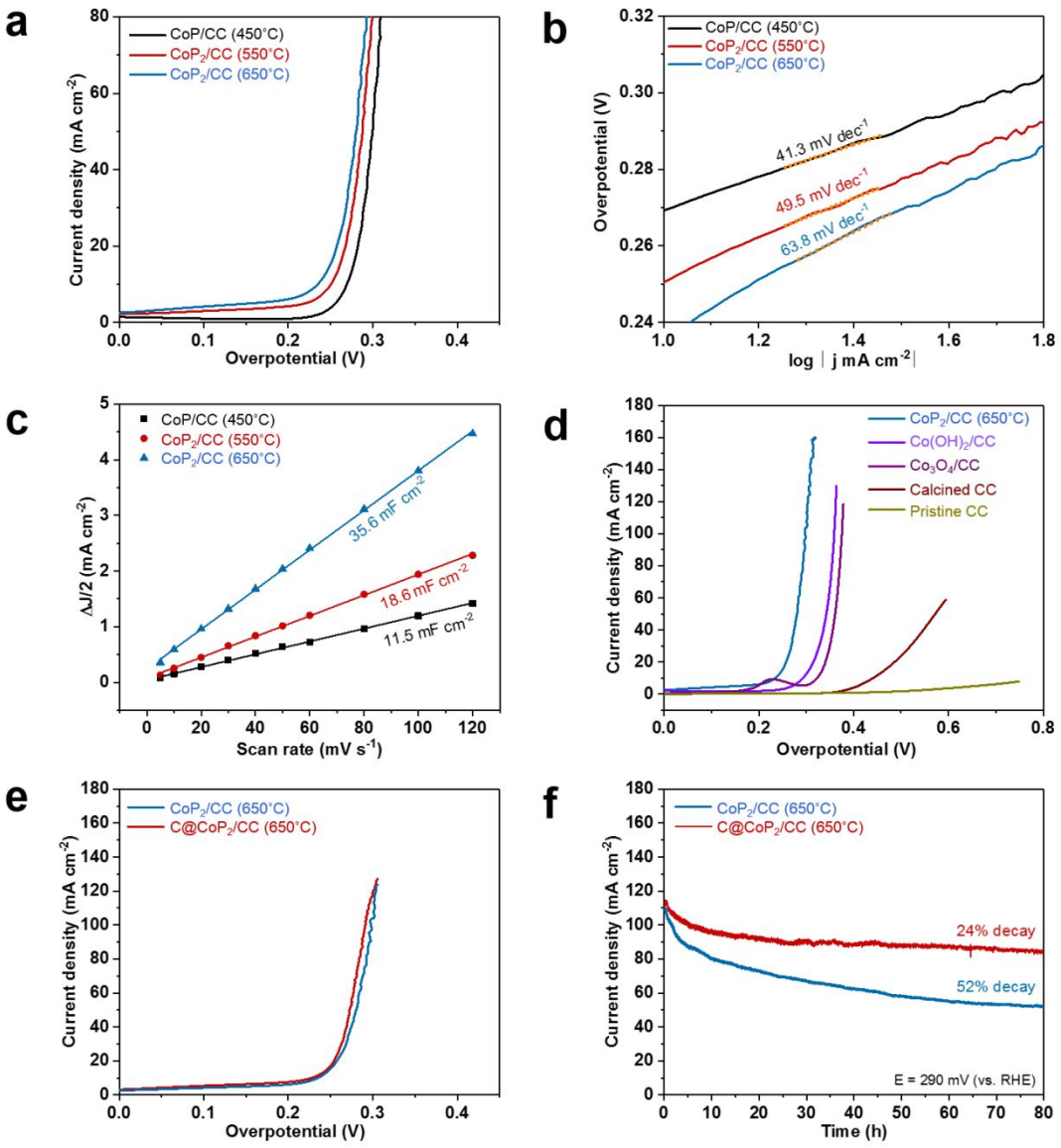

Figure 4. (a) Polarization curves for CoP_x/CC synthesized at different phosphidation temperatures, at a scan rate of 0.05 mV s^{-1} in 1 M $KOH_{(aq)}$ electrolyte solution. (b) Tafel slopes extracted from the polarization curves in (a). (c) Double-layer capacitance (Cdl) of CoP_x/CC synthesized at different phosphidation temperatures. (d) Polarization curves for CoP_2/CC formed at 650 °C, $Co(OH)_2$/CC, Co_3O_4/CC, calcined CC, and pristine CC at a scan rate of 0.05 mV s^{-1} in 1 M $KOH_{(aq)}$ electrolyte solution. (e) Polarization curves for pristine CoP_2/CC and C@CoP_2/CC formed at 650 °C with a scan rate of 0.05 mV s^{-1} in 1 M $KOH_{(aq)}$ electrolyte solution. (f) Time dependent performance of pristine CoP_2/CC and C@CoP_2/CC formed at 650 °C in 1 M $KOH_{(aq)}$ solution for 80 h at 0.85 V vs. Ag/AgCl.

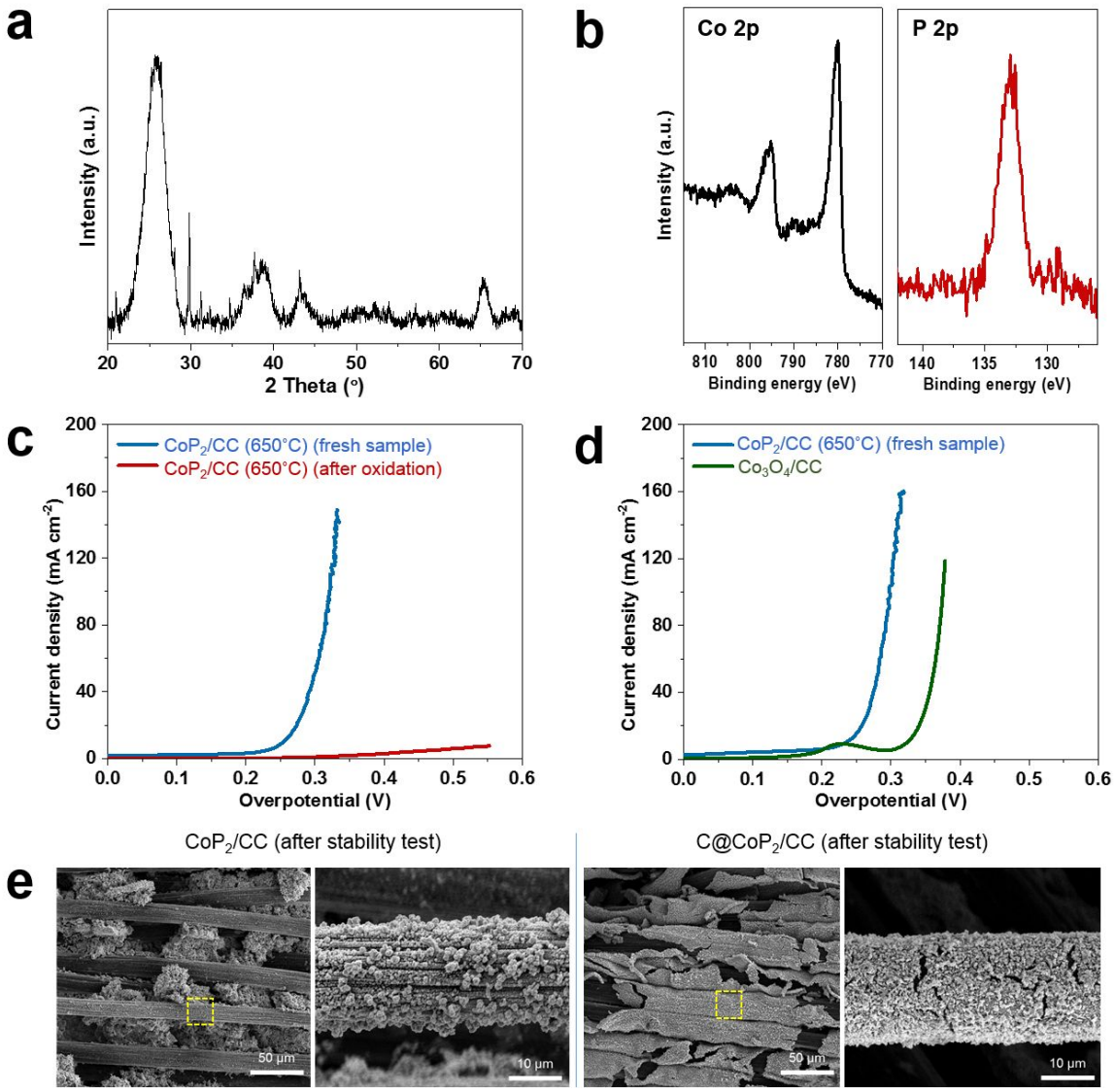

Figure 5. (a) Post-catalytic XRD patterns of CoP_2/CC (650 °C). (b) Post-catalytic Co 2p and P 2p XPS spectra for CoP_2/CC (650 °C). (c) Polarization curves before and after oxidation of CoP_2/CC formed at 650 °C at a scan rate of 0.05 mV s^{-1} in 1 M $KOH_{(aq)}$ electrolyte solution. (d) Polarization curves for CoP_2/CC (650 °C) and as prepared Co_3O_4/CC at a scan rate of 0.05 mV s^{-1} in 1 M $KOH_{(aq)}$ electrolyte solution. (e) SEM images of CoP_2/CC (left) and C@CoP_2/CC (right) after carrying out stability test for 60 hours. Specifically, the carbon shell effectively suppresses the dissociation of CoP_2 from CC, thus preserving the structural integrity and catalytic activity.

Table 1. Summary of OER metrics of the CoP_2/CC synthesized in this work along with state-of-art CoP_x catalysts reported in literature.

Catalyst	Substrate	η_{10} (mV)	Tafel slope (mV/dec)	Electrolyte	Reference
C@CoP_2	CC	234	64	1 M $KOH_{(aq)}$	This work
CoP NP/C	GCE	340	99	1 M $KOH_{(aq)}$	[19]
CoP NR/C	GCE	320	71	1 M $KOH_{(aq)}$	[19]
CoP_2/rGO	GCE	300	96	1 M $KOH_{(aq)}$	[29]
CoP/rGO-400	RDE	340	66	1 M $KOH_{(aq)}$	[22]
CoP_h/NG	CP	262	54	1 M $KOH_{(aq)}$	[17]
CoP nanoarrays	CC	281	119	1 M $KOH_{(aq)}$	[16]

Table of Contents